Biosensors and Bioelectronics 142 (2019) 111568

Contents lists available at ScienceDirect

Biosensors and Bioelectronics

journal homepage: www.elsevier.com/locate/bios

# Kinetics of lipid raft formation at lipid monolayer-bilayer junction probed by surface plasmon resonance

Yong-Sang Ryu[a,b], Hansik Yun[a], Taerin Chung[c], Jeng-Hun Suh[a], Sungho Kim[a], Kyookeun Lee[c], Nathan J. Wittenberg[d,e], Sang-Hyun Oh[d], Byoungho Lee[a], Sin-Doo Lee[a,c,*]

[a] School of Electrical and Computer Engineering, Seoul National University, 1 Gwanak-ro, Gwanak-gu, Seoul, 08826, South Korea
[b] Sensor System Research Center, Korea Institute of Science and Technology, Seongbuk-gu, Seoul, 02792, South Korea
[c] Inter-University Semiconductor Research Center, Seoul National University, 1 Gwanak-ro, Gwanak-gu, Seoul, 08826, South Korea
[d] Department of Electrical and Computer Engineering, University of Minnesota, 200 Union St SE, Minneapolis, MN, 55455, USA
[e] Department of Chemistry, Lehigh University, Bethlehem, PA, 18015, USA

ARTICLE INFO

*Keywords:*
Lipid raft
Lipid monolayer-bilayer junction
Real-time
Surface plasmon resonance
Optical sensors
Lipid-lipid interaction

ABSTRACT

A label-free, non-dispruptive, and real-time analytical device to monitor the dynamic features of biomolecules and their interactions with neighboring molecules is an essential prerequisite for biochip- and diagonostic assays. To explore one of the central questions on the lipid-lipid interactions in the course of the liquid-ordered ($l_o$) domain formation, called rafts, we developed a method of reconstituting continuous but spatially heterogeneous lipid membrane platforms with molayer-bilayer juntions (MBJs) that enable to form the $l_o$ domains in a spatiotemporally controlled manner. This allows us to detect the time-lapse dynamics of the lipid-lipid interactions during raft formation and resultant membrane phase changes together with the raft-associated receptor-ligand binding through the surface plasmon resonance (SPR). For cross-validation, using epifluorescence microscopy, we demonstrated the underlying mechanisms for raft formations that the infiltration of cholesterols into the sphingolipid-enriched domains plays a crucial roles in the membrane phase-separation. Our membrane platform, being capable of monitoring dynamic interactions among lipids and performing the systematic optical analysis, will unveil physiological roles of cholesterols in a variety of biological events.

## 1. Introduction

In cellular membranes, the formation of transient functional domains that spatially localize a set of particular lipids and proteins is a prerequisite for diverse membrane-associated biological activities such as cell signaling (Grecco et al., 2011; Hartman and Groves, 2011; Simons and Gerl, 2010; Thatcher, 2013), membrane deformation (Sakuma et al., 2010), and membrane trafficking (Ikonen, 2001; Sprong et al., 2001). In particular, sphingomyelin (SPM)- and cholesterol (CHOL)-enriched lipid raft-phases, known to be liquid ordered ($l_o$)-phase in vitro, have attracted much attention due to their critical roles in gathering pathogenic proteins related to a number of diseases including HIV (Lalonde and Sundquist, 2012), Prion (Critchley et al., 2004) and an Alzheimer's disease (Henderson et al., 2004; Jacobson et al., 2007; Lajoie and Nabi, 2010). To mimic cellular membranes, a supported lipid membrane (SLM) can serve as a model system to provide a biological membrane that can be interfaced with a solid surface for medical diagnostics and sensor applications. Using the SLM, the non-specific binding of biomolecules to the solid surface can be eliminated through the distribution of the membrane receptors within an inert background. Besides, the lateral mobilities of the membrane components are guaranteed to exploit how and why the raft-phases are activated through a number of surface-sensitive techniques (Groves, 2006; Groves and Boxer, 2002; Howland et al., 2005; Jeong et al., 2011; Okazaki et al., 2009; Ryu et al., 2015) However, owing to the spatiotemporal outbreaks of the raft domains in a random fashion, the physicochemical interactions among the raft-associated lipids and their kinetics during the raft formation have been poorly understood. From the experimental point of view, the real-time monitoring of the raft formation remains a long-standing challenging issue, leaving one of the central questions on the lipid-lipid interactions in the course of the $l_o$ domain formation.

To investigate $l_o$ domains, most of the techniques have relied upon fluorescence (FL)-labeled reporters. However, intrinsic properties of FL reporters tagged on target molecules prohibited an accurate data interpretation owing to the i) dye-dye interactions, ii) photobleaching, or

* Corresponding author. School of Electrical and Computer Engineering, Seoul National University, 1 Gwanak-ro, Gwanak-gu, Seoul, 08826, South Korea.
*E-mail address:* sidlee@plaza.snu.ac.kr (S.-D. Lee).

https://doi.org/10.1016/j.bios.2019.111568
Received 16 June 2019; Received in revised form 27 July 2019; Accepted 2 August 2019
Available online 10 August 2019
0956-5663/ 

iii) partitioning artifacts resulting from the conjugation of the FL moieties onto lipids (Groves, 2006; Rodrigo et al., 2018; Sezgin et al., 2012; Skaug et al., 2011; Veatch et al., 2007). As alternatives, for example, label-free lipid membrane-based surface plasmon resonance (SPR) techniques (Cooper, 2004; Homola et al., 1999; Jackman et al., 2017; Rich and Myszka, 2000; Šakanovič et al., 2019) have focused on measuring the binding events occurring between a membrane-bound receptors and soluble ligands such as proteins (Beseničar et al., 2006; Evans and Roger MacKenzie, 1999; Scarano et al., 2010) or DNA (Margheri et al., 2013) since they alleviate the artifacts associated with lipid fluorophores. Moreover, the SPR can measure the change of the interfacial refractive index (RI) by the structural change of the lipid phase in real-time (Salamon et al., 2005). However, in the presence of the spatiotemporally random outbreaks of the raft domains where optoelectronic signals are barely observable, the SPR techniques would suffer from the direct measurement of the kinetics of the lipid-lipid interaction that cause the $l_o$ domain formation (Fig. 1a) (Margheri et al., 2012, 2013). The very low population and the short lifetime of raft units (typically less than 1 ms) (Kusumi et al., 2004) leaves the real-time detection of raft domains as huge hurdles for bio-molecular sensing. To achieve a sufficient signal variation with an external stimulus in the SPR sensor, the accumulation of the raft units and their growth into micrometer-scale raft domains in high population are highly advantageous to monitor the lipid-lipid interactions by means of optical sensing. Thus, the development of a new SPR platform enabling the control of $l_o$ domain formation will unveil the raft organization kinetics.

Here, we report a unique and versatile membrane platform which enables to study the kinetics of the $l_o$ domain formation together with raft-associated receptor-ligand interactions by means of the simultaneous measurements of the time-lapse FL imaging and the SPR. Continuous but spatially heterogeneous membrane patches with different membrane compositions, *i.e.*, CHOL-rich SLMs amidst a background of SPM-rich SLMs, and their mixing to form the $l_o$ domains in desired regions (Fig. 1b) were realized through the combination of a micro-contact printing technique and the microfluidics. Our new platform enables to monitor the evolution of raft domains in time together with the kinetics of the sequential raft-participant receptor-ligand binding.

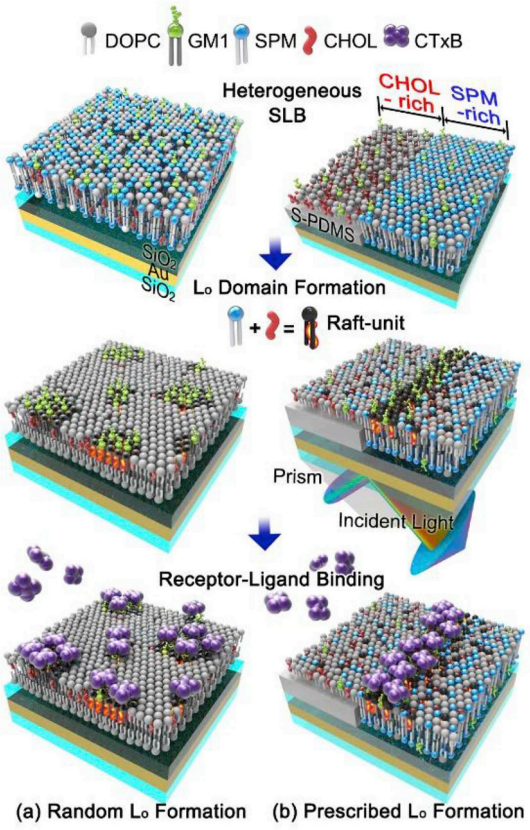


**Fig. 1. Random and prescribed $l_o$ domain formation in the SPR analysis** (a) Spatiotemporal random formation of $l_o$ domains on unpatterned substrate. The receptor ($GM_1$) for CTxB accumulates in $l_o$domains. (b) $L_o$ domains are directed to form at the junction between a CHOL-rich monolayer and a SPM-rich bilayer. $GM_1$ accumulates in the spatially pre-defined $l_o$ domain, and CTxB-$GM_1$ binding can be probed through the SPR by focusing the laser at the junction.

## 2. Materials and methods

### 2.1. Formation and imaging of supported lipid membrane

The phospholipids, used as a base for the formation of the SLMs, were 1,2-dioleoyl-sn-glycero-3-phophocholine (DOPC). For imaging the SLMs, negatively charged lipids labeled with red fluorescent dyes, Texas red 1,2-dihexadecanoyl-sn-glycero-3-phosphoethanolamine (TR-DHPE, ThermoFisher Scientific) were mixed with DOPC at 1 mol%. The sphingomyelin (SPM; brain, porcine), cholesterol (CHOL, ovine), and monosialoganglioside ($GM_1$; brain, ovine-ammonium salt) were purchase from Avanti Polar Lipids Inc, and they were mixed according to their purposes. All the lipid mixtures were dissolved in chloroform. The rapid solvent exchange method (Buboltz and Feigenson, 1999) was employed to evaporate chloroform and to hydrate with Tris buffer (100 mM NaCl and 10 mM Tris at pH 8.0) simultaneously. Small unilamellar vesicles (SUVs) were produced by extruding 20 times of the vesicle solution through a 50 nm filter (Avanti Polar Lipids). After the substrate was exposed to the SUV solution for 5 min, residual SUVs floating over a newly formed SLM were washed out in deionized (DI) water. The TR lipids were monitored using an epifluorescence microscopy (Eclipse E600-POL, Nikon) excited at appropriate wavelengths (EX 590 nm/EM 610 nm for Texas Red, EX 500 nm/EM 526 nm for Alexa Fluor 488, and EX 466 nm/EX 539 × nm for NBD, 10 × objective) and a He–Ne laser. All the experiments and measurements were performed at room temperature.

### 2.2. Fabrication of SPR sensing chip

The substrates of soda lime glass slides were cleaned in a piranha solution for 10 min, rinsed thoroughly with DI water, and dried using the gas flow of $N_2$. A 5-nm-thick Ti layer and a 50-nm-thick Au layer were then deposited on the substrate in sequence using an electron beam evaporator (KVE-3004, Korea Vacuum Corp.). For the SLM formation, an additional 40-nm-thick $SiO_2$ layer was subsequently prepared on the metal layer using the STS-PECVD equipment after an additional 5-nm-thick Ti layer (310PC, Surface Technology System). The prepared $SiO_2$-coated Au substrate was described together with the cross-sectional image of the SEM in the Supporting Information (Fig. S1).

### 2.3. Preparation of bifunctional PDMS microfluidic stamp

A glass substrate was immersed in acetone for at least 30 min, followed by rinsing in DI water for 10 min. The cleaning process was carried out using an ultra sonicator at room temperature. After the cleaned substrate was dried by the gas flow of $N_2$, negative photoresist (SU-8 2050, MICROCHEM) was spin-coated on the substrate to obtain a layer of 50 μm thick. The patterning of the substrate was carried out by the exposure of the ultraviolet (UV) light through a photomask using a mask aligner (MA-6, EVG). After photolithography, a silicone elastomer (Sylgard 184, Dow Corning Corp.), mixed with a curing agent at the ratio of 10:1, was poured onto a master mold and peeled off from it after at least 3 h at 80 °C on a hot plate. The fabricated microfluidic chips consisted of 100-μm-wide channels separated by either 100 μm

(Figs. 2 and 3) or 150 μm (SI Fig. S4).

### 2.4. Bifunctional role of PDMS stamps in formation of continuous monlayer-bilayer junction

The UV ozone treatment was performed on the SPR sensing chip to render the outermost surface more hydrophilic by producing hydroxyl (-OH) groups on the $SiO_2$ surface (Waring et al., 1999). Site selective surface modification was achieved through the stamping process of the micron-channel patterned polydimethylsiloxane (PDMS) mold onto the hydroxylated SPR chip at 200 °C for 3 min. Note that the stamped-PDMS (S-PDMS), yielding residual low-molecular-weight oligomers transferred from the PDMS mold, alters the surface property from being hydrophilic to hydrophobic (Briseno et al., 2006; Kim et al., 2014; Liu et al., 2009; Yang et al., 2009). This was previously demonstrated in the lipid monolayer architecture through the transfer of the S-PDMS to adjust the hydrophobicity using a thermally-assisted printing method (Kim et al., 2014; Suh et al., 2014). Details of the surface properties of the S-PDMS were described previously (Ryu et al., 2016b). The vesicle mixture was first injected along the micro channel to form the SLM. The peeling process was then performed to produce site-selective membrane patches of the lipid bilayers surrounded by S-PDMS regions. Subsequent backfilling of the vesicle mixture into the S-PDMS regions yields the secondary SLM and generates a continuous binary SLM which allows diffusive mixing across the lipid monlayer-bilayer junction.

### 2.5. SPR analysis of membrane film

The time-lapse SPR signals from the SLM samples were monitored in the Kretschmann configuration (Roh et al., 2011; Yuk and Ha, 2005). A sample plate was attached to a hemi-cylindrical prism (BK7; RI = 1.51) with a drop of index matching oil with RI = 1.51. The rotational stages (URS150BCC, Newport) were used to provide identical angles of both incidence and reflection (between 65° and 70°), former for a white light source and the other for a detector (an optical spectrum analyzer AQ6317B, Ando). The optimum SPR angle was determined by monitoring the reflected light intensity, of which shows minimum.

To achieve the SPR reflection data with respect to measured angles, the fitting of the second degree polynomials to the values for three pixels closest to the minimum was implemented, and then the minimum position for each film detection was calculated from the polynomial (Sjoelander and Urbaniczky, 1991). We used a relay-optics configuration (Yun et al., 2011) composed of three lenses and a polarizer so as to have a transverse magnetic field for the polarized light with directionality and to make a beam size as small as possible. Reflectance spectra were measured at wavelengths from 700 to 1200 nm. All measurements were performed at room temperature. For the calculation of the reflectance spectra together with the refractive indices of the samples in given structures, the custom-built rigorous coupled wave analysis (RCWA) tool was used (Kim et al., 2007, 2012).

## 3. Results and discussion

### 3.1. Membrane mixing at lipid MBJ

We describe the membrane mixing at the lipid MBJ in our fluidic channel with the SPR chip. The PDMS microfluidic mold was first attached to the $SiO_2$-covered Au substrate and a fluorescent bilayer (B) membrane was formed through the rupturing of the vesicles in the fluidic channels (Fig. 2a). The bilayer membranes appeared bright due to the presence of TR-DHPE in two leaflets of the membrane. Note that the B membranes were composed of the DOPCs doped with 1 mol% of TR-DHPEs for the FL imaging. Monolayer (M) membranes were subsequently formed on the S-PDMS regions by the additional SUV (label-free, pure DOPC) exposures as it bridges the M membrane to the upper leaflet of the adjacent B membrane, resulting in a continuous MBJ (Fig. 2b). The continuity of the MBJ was confirmed by membrane mixing, where the TR-DHPE from the B region (Fig. 2b; t = 0 min) freely diffuses into the M region (Fig. 2c; t = 5 min) until FL intensity distribution in each region approaches equilibrium. The brighter FL intensity over B regions than that over M regions clearly demonstrate the lipid mixing across the MBJ (Fig. 2d; t = 30 min). Also, distinct lateral fluidities of lipids in each region observed by the fluorescence recovery after photo-bleaching (FRAP) (Yee et al., 2004) obviously demonstrate different lipid architectures in B and M regions ($D_{Bi}$ = 1.43 ± 0.4 $\mu m^2/s$ for B region, whereas $D_{Mono}$ = 0.89 ± 0.3 $\mu m^2/s$ for the M region; see the SI Fig. S2). Together, S-PDMS provides the lipid junction between the lipid M and B architectures, and thus enable the diffusive lipids to cross distinct lipid architectures.

### 3.2. $L_o$ domain formation at pre-defined area

For the SPR monitoring of the $l_o$ domain formation and sequential protein bindings, it is crucial to form $l_o$ domains at predefined locations onto which the SPR laser can be focused. To accomplish this, we exploited the tight association of SPM and CHOL molecules to form $l_o$-units by first depositing a fluorescent B membrane rich in SPM (SPM/DOPC/$GM_1$/TR-DHPE = 33/65/1/1), then backfilling with a CHOL-rich M membrane (CHOL/DOPC/$GM_1$/TR-DHPE = 33/65/1/1). The

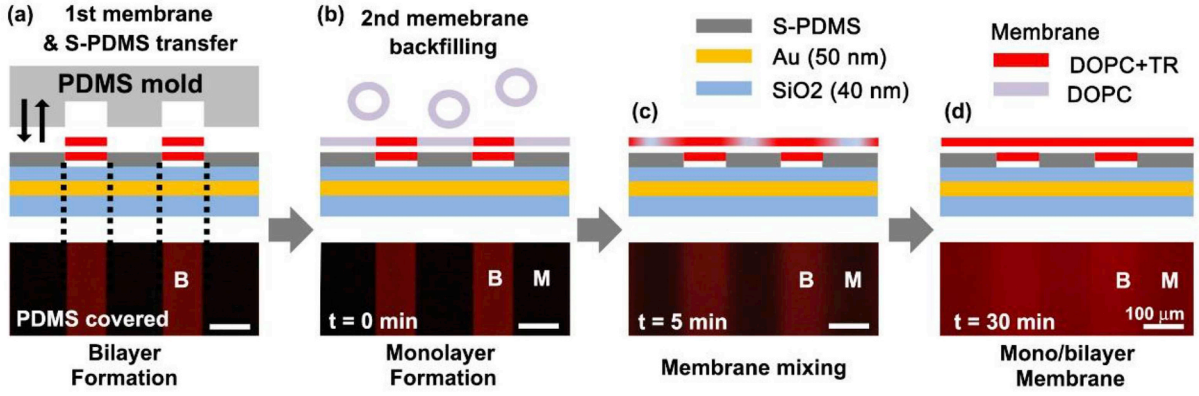


**Fig. 2. Membrane mixing at lipid monolayer-bilayer junction (MBJ)** The PDMS microfluidic mold was first attached to the $SiO_2$-over-Au substrate and a fluorescent bilayer membrane (B) was formed by rupturing vesicles in the channels (a). The PDMS mold was then removed to leave only the stamped-PDMS (S-PDMS) surface where label-free lipid monolayers (M) were formed (b). After 5 min, the fluorescence began to broaden due to the diffusion of the fluorescent probe (TR) into the monolayer from the top leaflet of the bilayer (c). After 30 min, the fluorescence was fully spread out in the entire monolayer (d). The bilayer membrane remained brighter due to the presence of TR in two leaflets of the membrane.

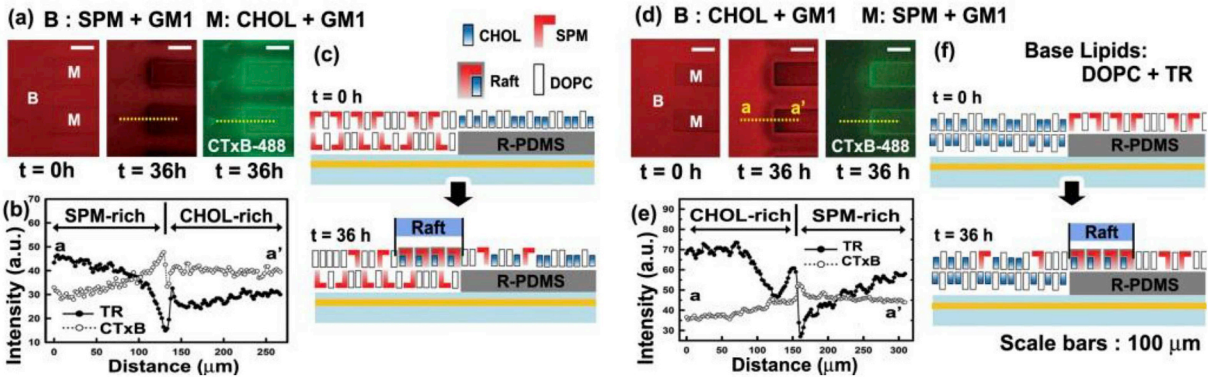


**Fig. 3. Formation of $l_o$ domains at pre-defined MBJ through the diffusion of CHOLs into SPM-rich membrane** (a) Pre-patterned MBJ before ($t$ = 0 h) and after $l_o$ domain formation ($t$ = 36 h) showing the depletion of TR at MBJ boundary. The bilayer was SPM-rich (SPM/DOPC/$GM_1$/TR = 33/65/1/1) whereas the monolayer was rich in CHOL (CHOL/DOPC/$GM_1$/TR = 33/65/1/1). Exposure to CTxB-488 showed that $GM_1$ was enriched in the $l_o$ domain in the bilayer (SPM-rich) side of the MBJ. (b) Intensity profiles corresponding to TR and CTxB-488 fluorescence along the dotted line shown in (a). (c) Illustration of the coalescence of $l_o$ domains in the bilayer due to the association of SPM with CHOL. (d) Fluorescence image of the MBJ where the bilayer was CHOL-rich and the monolayer was SPM-rich. (e) Intensity profiles corresponding to TR and CTxB-488 fluorescence along the dotted line (a-a') shown in (d). (f) Illustration of the coalescence of $l_o$ domains in the monolayer due to the diffusion of CHOLs into SPM-rich domain.

presence of $l_o$ domains can be determined by their well-characterized exclusion of the TR fluorophore. Basically, the molecular compaction between the SPM and the CHOL through the strong molecular binding affinity leads to the FL-free $l_o$ phase formation by expelling the DOPCs and the TR-DHPEs from the $l_o$ domains into the $l_d$ domains. The distinct physical properties of the $l_d$ phase, thicker by about 1 nm and higher in the spontaneous curvature than the $l_d$ phase, accelerate the formation of micrometer-scale $l_o$ domains surrounded by the $l_d$ domains (Ryu et al., 2015; Yoon et al., 2006). Interestingly, we found that $l_o$ domains are preferentially formed at the M/B boundary with a slight bias toward the SPM-rich side of the MBJ. After 36 h, a FL intensity profile of TR around the MBJ regions gradually increases with distance into the SPM-rich region, indicating that $l_o$ domains initially form at the MBJ then slowly coarsen within the SPM-region as time passes (Fig. 3a). Since successive gathering of newly formed nanorafts (SPM-CHOL units) at the boundary of the MBJ (especially, for the SPM-rich side) generates a concentration gradient of the CHOL and the SPM from the BMJ (high) to the SPM-enriched membrane (low). This is consistent with the experimental data of the fluorescence (FL) intensity by the TR-DHPE from the CHOL-enriched region (high) to the SPM-enriched region (low), showing the sharp increase of the FL intensity with approaching the CHOL-rich side (Fig. 3a and d). It indeed supports our assumption that the infiltration of the CHOLs into the SPM rich domain is the physical origin of the direction-sensitive $l_o$ domain formation. Note that the lipid mixing occurs at the MBJ, not only for the CHOL transfer but also for the $l_d$ phase (DOPC and TR-DHPE) through the outer leaflet of the supported lipid membrane. Binding of Alexa Fluor 488-labeled cholera toxin B subunit (CTxB-488), a marker for $GM_1$, shows that $GM_1$ is enriched in the $l_o$ domains, in agreement with prior studies (Ryu et al., 2014; Yoon et al., 2006). Figure 3b shows the FL intensity profiles of TR and CTxB-488 along the yellow dotted lines (Fig. 3a). This plot further illustrates the exclusion of TR from the $l_o$ domain at the MBJ, as well as an enrichment of $GM_1$. Details of the molecular dynamics investigating how and why the $l_o$ domains are preferentially localized at the SPM-rich side will be pursued together with specific applications of our label-free sensing platform. In short, the observed extension of the $l_o$ domain into the SPM-rich B membrane could be explained by the mechanism shown in Fig. 2c. Once membrane mixing occurs, the CHOLs from the M region diffuse into and intercalates with the SPM rich B membrane, and induce molecular compaction to form $l_o$-units. To test our assumption, we carried out the diametric experiment where the B membrane with CHOL-rich (CHOL/DOPC/$GM_1$/TR = 33/65/1/1) and the backfilled M membrane was CHOL-free but contained SPM-rich (SPM/DOPC/$GM_1$/TR = 33/65/1/1). In this case, the $l_o$ domain preferentially formed on the SPM-rich M membrane side of the M/B boundary (Fig. 3d). This obviously represents that the nanoraft coarsening process began at the MBJ and proceeded to extend toward the SPM-rich M membrane over the course of 36 h, and being confirmed by the binding of the CTxB-488 (Fig. 3d). The FL intensity profiles (Fig. 3e) support the notion that intercalation of CHOLs into SPM-rich membranes drives $l_o$ domain formation (Fig. 3f). These comparative experiments obviously demonstrated that reliable and controlled positioning of the $l_o$ domains can be achieved through the MBJ platform, which facilitates optical detections for monitoring of the kinetics of lipid raft formation (see the SI Fig. S3).

### 3.3. Kinetics of lipid-lipid interaction and protein binding

Having established that $l_o$ domains initiate and assemble around the MBJ, we monitored the time-lapse kinetics of the $l_o$ domain assembly and subsequent protein binding events using the SPR. Note that the SPR laser was focused on a spot that encompassed the M and B regions including the MBJ (SI Fig. S3a). Figure 4a represented steady-state normalized SPR reflectance spectra with diverse resonance dips in a variety film conditions with respect to the measured spectrum of air/$SiO_2$ interface (black circles). A dramatic resonance red-shift was monitored when phosphate buffer solution (PBS, pH 7.4) is injected to air/$SiO_2$ interface through microfluidic PDMS channels, as shown with the minimum dip of about 790 nm (red circles). Next, a SPM-rich bilayer membrane was formed resulting in resonance red shifted about 20 nm (~810 nm, green triangles) due to the increased interfacial RI. After peeling off the PDMS fluidic channels in an aqueous environment, the chip was backfilled with CHOL-rich vesicle mixtures to form a monolayer on the S-PDMS surface, which had minimal effect on the resonance position (yellow triangles). Note that washing processes were conducted to leave the lipid membrane without floating residual vesicles in an aqueous environment. After 20 h of membrane mixing, interestingly, additional RI changes were monitored as represented by ~5 nm of signal red shifts (blue squares). To test if the 5 nm of resonance shifts was likely due to increased lipid packing density and membrane thickness changes associated with a $l_o$ domain formation at the MBJ boundary, we coupled time-lapse SPR measurements with FL microscopy. The time-lapse measurements of minimum position of resonance dips at each step were measured by polynomial curve fitting of SPR signal (Sjoelander and Urbaniczky, 1991) (Fig. 4b). The period 'I' (0 h < t < 1.4 h) represents the formation of bilayer SLM rich in SPMs, followed by lipid backfilling in form of monolayer SLM rich in CHOLs (Fig. 4c). The resonance spectra during membrane mixing and resultant $l_o$ domain formation at the MBJ were represented in period 'II'

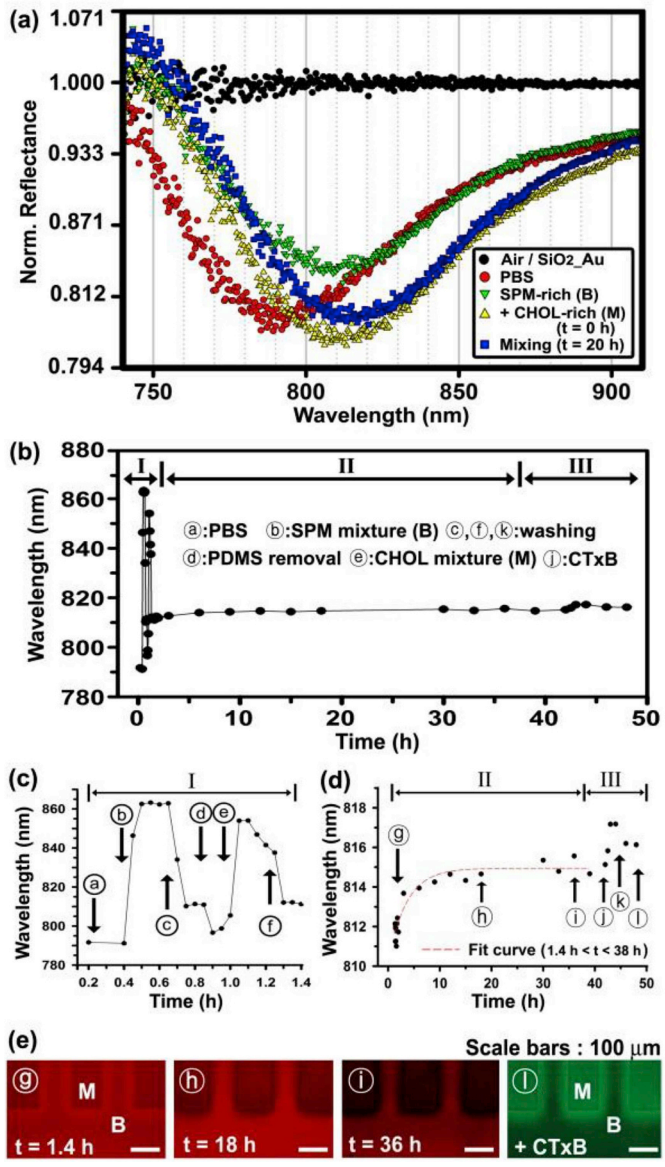


**Fig. 4. Kinetics of dye-labeled membrane reorganization and protein binding** (a) Steady-state SPR spectra recorded without (black ●) and with (red ●) PBS solution; after the formation of the SPM-rich bilayer membrane (green ▼); after the formation of the CHOL-rich lipid monolayer (yellow ▲; $t$ = 0 h); and after the membrane mixing for 20 h (blue ■; $t$ = 20 h). (b) The shift of the SPR as a function of time during the formation of the SPM-rich bilayer and the CHOL-rich monolayer (I), in reorganization of the membrane to form $l_o$ domains (II), and in binding of CTxB to $GM_1$ (III). (c) Magnified view of the SPR signal during period I where the monolayer (M) and bilayer (B) membranes were formed. (d) Magnified view of the SPR signal during period II and period III where the $l_o$ domain was assembled (II) and CTxB was injected and bound to $GM_1$ (III). (e) Fluorescence images of the M and B membranes at different times. In the figures from (b)–(d), the same character symbol in circle represents the same case. (For interpretation of the references to colour in this figure legend, the reader is referred to the Web version of this article.)

(1.4 h < t < 42 h). Finally, the peak shift by the ligand-receptor specific binding (i.e., CTxB-$GM_1$) is also measured in period 'III' (42 h < t < 50 h). The circled letters (Fig. 4c) correspond to the legend (Fig. 4b). A sharp shift in resonance was monitored when the SPM-rich vesicles were injected through PDMS channel, ⓑ, followed by a sharp blue-shift during washing process,ⓒ. After residual vesicle removal, the resultant resonance dip was slightly red-shifted (790→810 nm) compared to the signal before the vesicle injection, ⓐ, which indicates the formation of B membrane. After microfluidic removal, ⓓ, the CHOL-rich vesicles were injected, ⓔ, followed by another washing step, ⓕ. The large change in resonance wavelength after vesicle injection steps, ⓑ and ⓔ, is attributed to the sensing of both newly formed SLMs and floating vesicles within probing depth ranges. Also the temporal wavelength drop between ⓓ and ⓔ steps were caused by SPR measurement of partially lipid-free area (= S-PDMS region) together with existence of SPM-rich B membrane. After the final washing step, ⓕ, the resonance wavelength is shifted about 20 nm compared to the resonance dips before membrane formation, ⓐ, which clearly demonstrate the deposition of SLM over the SPR sensing areas of interest.

The magnified analysis of $l_o$ domain formation resulting from the lipid mixing across the MBJ (period II), and subsequent CTxB binding to a raft-associated $GM_1$ lipids (period III) are represented (Fig. 4d). Interestingly, the time-lapse measurement of SPR signals in period II shows about 5 nm of red-shift of wavelength dip in a curvilinear shape (from the initial state, ⓖ, to the plateau, ⓗ) which agrees with results of Moore et al. (2006). To confirm the existence of raft-associated $GM_1$ clusters in $l_o$ domains, the phase-separated chip was exposed to the CTxB-488 for 2 h (ⓙ, t = 42–44 h), followed by complete washing process (ⓚ, t = 44 h) to remove unbound CTxB-488 (period III). This clearly showed about 2 nm of additional resonance red-shift which implies an increase of interfacial RI. The signal correspondent FL images of the SLM with different level of $l_o$ domain phase-separation at various time points (Fig. 4e, ⓖ-ⓘ and ⓘ) were also observed to facilitate the interpretation form SPR signal changes related to the molecular compactions and dynamics. For example, the $l_o$ domain formation was confirmed by the TR lipid depletion; both in M (CHOL-rich) membrane and slightly toward B (SPM-rich) membrane. As clearly shown in Fig. 4eⓘ, the dimmer FL intensity at the B regions arose from the $l_o$ domain formation by intercalation of CHOLs to SPM-rich SLM domain. Note that darker FL profiles in M regions are attributed to the preferential localization of $l_o$ domain-units in hydrophobic-hydrophobic interfacial interaction between lipids and substrate surface, which were recently reported (Ryu et al., 2016b). Although different mechanisms drove $l_o$ domain formations in each M and B region (ⓘ, Fig. 4e), it is clear that the binding of the CTxBs, especially where less FL profiles were probed, demonstrates localized $l_o$ domain formation as it also shows great performance of receptor-ligand binding events between $GM_1$ and CTxBs (ⓘ, Fig. 4e). From the time-lapse SPR data accompanied with corresponding FL micrographs, we are able to conclude that the 5-nm-shift of curvilinear-shaped SPR signal (Fig. 4d, ⓖ-ⓘ) results from the $l_o$ domain formation, while 2-nm-shift arise from ligand-receptor binding ($GM_1$-CTxB, Fig. 4d, ⓙ-ⓘ). Taken together, the combinatory analysis by FL data with SPR signals enables to visualize the spatial distribution of $l_o$ domains concurrently on detection of the RI changes associated with $l_o$ domain formation and protein binding to raft-associated receptors.

### 3.4. Label-free membrane reorganization and their protein binding

Under certain conditions, lipid fluorophores can alter $l_o$ domain formation and influence the phase partitioning behavior of other lipids and protein binding activity (Sezgin et al., 2012; Zhao et al., 2007). For this reason, we carried out SPR experiments in the absence of TR-DHPEs and compared the SPR response to signals from SLMs containing TR-DHPEs. In this experiment the FL label-free, SPM-enriched B membranes (SPM/DOPC/$GM_1$ = 33/66/1) and the CHOL-enriched M membranes (CHOL/DOPC/$GM_1$ = 33/65/1) were prepared. The SPR resonance shift as a function of time for the TR-free membranes showed a slightly decreased maximum shift, compared to samples containing TR-DHPEs (Fig. 5a). The slight difference in SPR response is attributed to the lack of TR-DHPEs, which has a bulky FL moiety that could subtly influence the interfacial RI. The specific-binding of protein (CTxB-488) to phase-separated unlabeled membranes was also tested (Fig. 5b). Here, the evolution of SPR reflectance spectra clearly shows that phase-

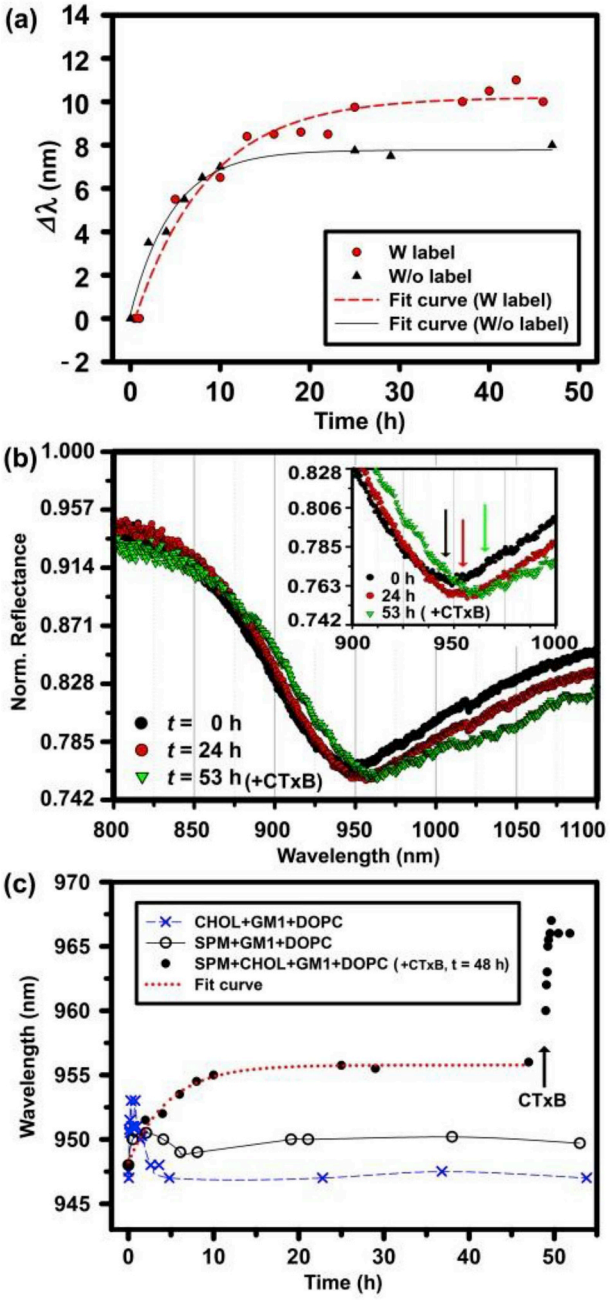


**Fig. 5. Kinetics of label-free membrane reorganization and protein binding** (a) Comparison of real-time SPR signals during self-assembling $l_o$ domains for two membranes with and without the TR fluorophore in the raft mixture (CHOL/SPM/DOPC/$GM_1$). The solid and dashed lines were the fits of the data to Eq. (2). (b) SPR reflectance spectra recorded before ($t$ = 0 h) and after ($t$ = 24 h) the phase separation, followed by the binding of CTxB (t = 53 h) to the $l_o$ domain. (c) Comparison of the SPR response in the membrane with either CHOLs ( × ) or SPMs (○), but not both, as well as the membrane containing both SPM and CHOL (•). The data were fitted to Eq. (2). The other two curves (black solid and blue dashed) connecting the data points were simply the guides for the eye. The membrane with both SPM and CHOL was subsequently exposed to CTxB at the time ($t$ = 50 h) indicated by the black arrow. (For interpretation of the references to colour in this figure legend, the reader is referred to the Web version of this article.)

separated label-free membrane (t = 0–48 h) and binding of 25 μg/ml of CTxB-488 to $GM_1$ (t = 53 h) was successfully achieved in a label-free fashion. The distribution of CTxB-488 on label-free heterogeneous SLMs confirms that spatially phase-separated $l_o$ domains were formed at the MBJ (SI Fig. S4). We also test the influence of compositional variations in $l_o$ domains and monitored the SPR time-lapse evolution of wavelength signal without the fluorophore TR. Different from the time-lapse evolution of wavelength in curvilinear-shaped red-shift by both SPM and CHOL included SLMs, the SPR signals from a SPM-free membrane (CHOL/DOPC/$GM_1$ = 33/66/1) or a CHOL-free membrane (SPM/DOPC/$GM_1$ = 33/66/1) in both M and B regions shifted much less or remain rather constant (Fig. 5c). It is widely known that the presence of SPM or CHOL alone at these mole fractions does not induce $l_o$ domain formation (Lee et al., 2014; Ryu et al., 2014), therefore we attribute the curvilinear shift in SPR signal to the coalescence of $l_o$ domains. The SPMs and CHOLs can associate to form nanoscale $l_o$-units, and subsequent lipid mixing through the MBJ can serve to coarsen $l_o$ domains to the micrometer scale, which leads to a change in interfacial RI causing red-shift in the SPR reflectance spectrum.

The curvilinear shift in SPR signal can be fit using a first order reaction model (Vijayendran et al., 1999), where two molecules associate to form product complexes ($l_o$-units). This can be expressed as

$$\text{SPM} + \text{CHOL} \rightarrow l_o\text{-unit} \quad (1)$$

The integrated rate equation for $l_o$-unit formation as a function of time, P(t), can be written as

$$P(t) = P_\infty(1\text{-}e^{-kt}) \quad (2)$$

Here, $P_\infty$ represents the amount of product ($l_o$-units) at equilibrium and k is the association rate constant. According to Eq. (2), the amount of $l_o$-unit complexes increases with time until the supply of reactants (CHOL and SPM) is exhausted, which occurs at the MBJ in our case. Once $l_o$-unit complexes are formed they coarsen and form micron-scale $l_o$ domains in order to release energetically unfavorable height mismatch between the $l_o$ domains and liquid-disordered ($l_d$) domains (García-Sáez et al., 2007). The coarsening of the $l_o$ domain causes thicker, more ordered and more densely-packed membranes when compared to those of $l_d$ domains, which is probed by the SPR (Fig. 5c). By fitting the SPR signal shift to Eq. (2), we were able to extract a value for the rate constant of k = 0.212 $h^{-1}$. The rate of $l_o$ domain coalescence is most likely limited by the 2-dimensional lipid diffusion in the planar membrane showing smaller binding coefficient on binding kinetics. In our system, the $l_o$ domains only assembled in SPM-rich regions, which we attribute to the CHOL intercalating with the SPM clusters to form $l_o$ domains (Figs. 3c and f). Assuming a constant membrane thickness in our system, the observed SPR shift of about 8 nm (948→956 nm, Fig. 4c) during $l_o$ domain formation might be indicative of changes in the membrane physical properties, such as increased packing density, which agrees with other works (Ryu et al., 2014; Yoon et al., 2006) showing that $l_o$ domains are more ordered and densely packed than $l_d$ domains. While the observed SPR shifts are not definitive evidence of molecular association between CHOLs and SPMs, we can use SPR to deduce that $l_o$ domain formation does change the RI of the membrane in the SPR observation area. For example, by assuming the SPM-rich B membrane has a thickness of 4.6 nm (Henderson et al., 2004), we can calculate a RI of the B membrane of RI = 1.52, which agrees well with earlier work of Salamon et al. (2005). Intercalation of CHOL into SPM-rich membrane by the membrane mixing at MBJ induces molecular compaction in between SPM and CHOL, defined as '$l_o$-unit', and this successive genesis of the $l_o$-units is likely to assemble in forms of $l_o$ domains in order to release membrane energies (Ryu et al., 2014; Yoon et al., 2006), causing an additional resonance shift of about 8 nm. This value corresponds to a RI change of membrane from RI = 1.52 to 1.60 based on the fact that CHOL's intercalation doesn't alters membrane thickness (Sprong et al., 2001). Note that a home-built rigorous coupled wave analysis (RCWA) package was used for the calculation (Kim et al., 2007, 2012). The substrate platform and instrumental system described here can monitor both the dynamic and equilibrium states of the $l_o$ domain formation and provide significant

clues for understanding $l_o$ domain formation in heterogeneous membrane systems. This system provides a platform to create fluid, contiguous membranes across heterogeneous substrates, which overcomes the membrane discontinuities typically observed on substrates with patterned polymers (Ryu et al., 2012, 2016a), proteins (Kung et al., 2000), or lipid-free gap (Howland et al., 2005). Based on our finding that CHOLs majorly diffuse into SPM-rich domain, our systematic platform enables $l_o$ domain formation to form in controlled areas, which simplifies analysis with FL microscopy, but more significantly, facilitates SPR analysis of lipid reorganization and toxin/ganglioside interactions (Margheri et al., 2012, 2013).

## 4. Conclusion

We demonstrated a new approach to the optically sensitive, label-free detection of biological activities in continuous but spatially heterogeneous lipid membrane. Based on the SPR sensor architecture, we monitored the kinetics of lipid-lipid interactions during the raft domain coalescence, from the appearance of the $l_o$ phase to its growth into a micrometer-scale $l_o$ domain through self-assembling, followed by the binding of a protein toxin to raft-associated ganglioside receptors. In accurately determining the physical parameters (*i.e.*, RI and lipid packing density) of the $l_o$ domain, it is necessary to use a laser spot smaller than the size of the $l_o$ domain in the SPR sensor. The location of the $l_o$ phase in the MBJ is critical for achieving a sufficient change of the SPR signal to explore the kinetics of the raft domain genesis. Our sensor architecture enables to localizate the raft domains at specific positions in a programmed manner for precise optical sensing measurements. In principle, our SPR platform could be expanded to unveil the roles of particular lipids and their interactions with raft-associated pathogenic proteins causing a number of diseases (e.g., HIV, Prion, Alzheimer's disease etc.). It can be applied to monitor other important biomolecules (DNA or viruses) that interact with membranes, for example, in a number of different fields such as drug discovery (Bayley and Cremer, 2001), proteomics (Winssinger et al., 2001), analytical chemistry, and materials engineering. From the methodological point of view, our approach will be integrated with label-free surface-based detection methods such as Raman spectroscopy or multi-resonant infrared measurements, and Terahertz spectroscopy (Lee et al., 2018; Rodrigo et al., 2018).

*Notes*

The authors declare no competing financial interest.

## Declaration of competing interest

The authors declare that they have no known competing financial interests or personal relationships that could have appeared to influence the work reported in this paper.

## CRediT authorship contribution statement

**Yong-Sang Ryu:** Conceptualization, Data curation, Validation, Writing - original draft, Writing - review & editing. **Hansik Yun:** Conceptualization, Data curation, Formal analysis, Software, Methodology, Writing - original draft. **Taerin Chung:** Conceptualization, Data curation, Formal analysis. **Jeng-Hun Suh:** Conceptualization, Software, Methodology, Validation, Visualization. **Sungho Kim:** Conceptualization, Data curation, Formal analysis. **Kyookeun Lee:** Conceptualization, Software, Methodology. **Nathan J. Wittenberg:** Validation, Writing - original draft. **Sang-Hyun Oh:** Funding acquisition, Writing - original draft. **Byoungho Lee:** Conceptualization, Data curation, Validation, Funding acquisition. **Sin-Doo Lee:** Conceptualization, Data curation, Validation, Funding acquisition, Writing - original draft, Writing - review & editing.

## Acknowledgements

This work was supported in part by KIST intramural grants (#2E29530, #2V07430, and #2E29475), the National Research Foundation, and BK 21 Plus Program funded by the Ministry of Education of Korea. N.J.W. and S.-H.O. acknowledge support from the Minnesota Partnership for Biotechnology and Medical Genomics.

## Appendix A. Supplementary data

Supplementary data to this article can be found online at https://doi.org/10.1016/j.bios.2019.111568.

## References

Bayley, H., Cremer, P.S., 2001. Nature 413 (6852), 226–230.
Beseničar, M., Maček, P., Lakey, J.H., Anderluh, G., 2006. Chem. Phys. Lipids 141 (1), 169–178.
Briseno, A.L., Roberts, M., Ling, M.M., Moon, H., Nemanick, E.J., Bao, Z.N., 2006. J. Am. Chem. Soc. 128 (12), 3880–3881.
Buboltz, J.T., Feigenson, G.W., 1999. Biochim. Biophys. Acta 1417 (2), 232–245.
Cooper, M.A., 2004. J. Mol. Recognit. 17 (4), 286–315.
Critchley, P., Kazlauskaite, J., Eason, R., Pinheiro, T.J.T., 2004. Biochem. Biophys. Res. Commun. 313 (3), 559–567.
Evans, S.V., Roger MacKenzie, C., 1999. J. Mol. Recognit. 12 (3), 155–168.
García-Sáez, A.J., Chiantia, S., Schwille, P., 2007. J. Biol. Chem. 282 (46), 33537–33544.
Grecco, H.E., Schmick, M., Bastiaens, Philippe I.H., 2011. Cell 144 (6), 897–909.
Groves, J.T., 2006. Science 313 (5795), 1901–1902.
Groves, J.T., Boxer, S.G., 2002. Acc. Chem. Res. 35 (3), 149–157.
Hartman, N.C., Groves, J.T., 2011. Curr. Opin. Cell Biol. 23 (4), 370–376.
Henderson, R.M., Edwardson, J.M., Geisse, N.A., Saslowsky, D.E., 2004. Physiology 19 (2), 39–43.
Homola, J., Yee, S.S., Gauglitz, G., 1999. Sens. Actuators B Chem. 54 (1), 3–15.
Howland, M.C., Sapuri-Butti, A.R., Dixit, S.S., Dattelbaum, A.M., Shreve, A.P., Parikh, A.N., 2005. J. Am. Chem. Soc. 127 (18), 6752–6765.
Ikonen, E., 2001. Curr. Opin. Cell Biol. 13 (4), 470–477.
Jackman, J.A., Ferhan, A.R., Cho, N.-J., 2017. Chem. Soc. Rev. 46 (12), 3615–3660.
Jacobson, K., Mouritsen, O.G., Anderson, R.G.W., 2007. Nat. Cell Biol. 9 (1), 7–14.
Jeong, C., Lee, S.-W., Yoon, T.-Y., Lee, S.-D., 2011. J. Nanosci. Nanotechnol. 11 (5), 4527–4531.
Kim, H., Lee, I.-M., Lee, B., 2007. J. Opt. Soc. Am. A 24 (8), 2313–2327.
Kim, H., Park, J., Lee, B., 2012. Fourier Modal Method and its Applications in Computational Nanophotonics. CRC Press.
Kim, S., Ryu, Y.-S., Suh, J.-H., Keum, C.-M., Sohn, Y., Lee, S.-D., 2014. J. Nanosci. Nanotechnol. 14 (8), 6069–6071.
Kung, L.A., Kam, L., Hovis, J.S., Boxer, S.G., 2000. Langmuir 16 (17), 6773–6776.
Kusumi, A., Koyama-Honda, I., Suzuki, K., 2004. Traffic 5 (4), 213–230.
Lajoie, P., Nabi, I.R., 2010. Int. Rev. Cell Mol. Biol. 282, 135–163.
Lalonde, M.S., Sundquist, W.I., 2012. Proc. Natl. Acad. Sci. U.S.A. 109 (46), 18631–18632.
Lee, D.-K., Yang, H., Song, H.S., Park, B., Hur, E.-M., Kim, J.H., Park, T.H., Seo, M., 2018. Sens. Actuators B Chem. 273, 1371–1375.
Lee, H., Park, W., Ryu, H., Jeon, N.L., 2014. Biomicrofluidics 8 (5), 054102.
Liu, K., Tian, Y., Pitchimani, R., Huang, M., Lincoln, H., Pappasa, D., 2009. Talanta 79 (2), 333–338.
Margheri, G., D'Agostino, R., Becucci, L., Guidelli, R., Tiribilli, B., Del Rosso, M., 2012. Biomed. Opt. Express 3 (12), 3119.
Margheri, G., D'Agostino, R., Del Rosso, M., Trigari, S., 2013. Lipids. pp. 1–9.
Moore, D.J., Snyder, R.G., Rerek, M.E., Mendelsohn, R., 2006. J. Phys. Chem. B 110 (5), 2378–2386.
Okazaki, T., Tatsu, Y., Morigaki, K., 2009. Langmuir 26 (6), 4126–4129.
Rich, R.L., Myszka, D.G., 2000. Curr. Opin. Biotechnol. 11 (1), 54–61.
Rodrigo, D., Tittl, A., Ait-Bouziad, N., John-Herpin, A., Limaj, O., Kelly, C., Yoo, D., Wittenberg, N.J., Oh, S.-H., Lashuel, H.A., 2018. Nat. Commun. 9 (1), 2160.
Roh, S., Chung, T., Lee, B., 2011. Sensors 11 (2), 1565–1588.
Ryu, Y.-S., Lee, I.-H., Suh, J.-H., Park, S.C., Oh, S., Jordan, L.R., Wittenberg, N.J., Oh, S.-H., Jeon, N.L., Lee, B., 2014. Nat. Commun. 5, 4507.
Ryu, Y.-S., Lee, S.-W., Lee, B., Lee, S.-D., 2012. Mol. Cryst. Liq. Cryst. 559 (1), 1–8.
Ryu, Y.-S., Suh, J.-H., Kim, M.-H., Sohn, Y., Lee, S.-D., 2016a. J. Nanosci. Nanotechnol. 16 (6), 6355–6359.
Ryu, Y.-S., Wittenberg, N.J., Suh, J.-H., Lee, S.-W., Sohn, Y., Oh, S.-H., Parikh, A.N., Lee, S.-D., 2016b. Sci. Rep. 6, 26823.
Ryu, Y.-S., Yoo, D., Wittenberg, N.J., Jordan, L.R., Lee, S.-D., Parikh, A.N., Oh, S.-H., 2015. J. Am. Chem. Soc. 137 (27), 8692–8695.
Šakanovič, A., Hodnik, V., Anderluh, G., 2019. Surface Plasmon Resonance for Measuring Interactions of Proteins with Lipids and Lipid Membranes, Lipid-Protein Interactions. Springer.
Sakuma, Y., Taniguchi, T., Imai, M., 2010. Biophys. J. 99 (2), 472–479.
Salamon, Z., Devanathan, S., Alves, I.D., Tollin, G., 2005. J. Biol. Chem. 280 (12), 11175–11184.
Scarano, S., Mascini, M., Turner, A.P.F., Minunni, M., 2010. Biosens. Bioelectron. 25 (5),

957–966.
Sezgin, E., Levental, I., Grzybek, M., Schwarzmann, G., Mueller, V., Honigmann, A., Belov, V.N., Eggeling, C., Coskun, Ü., Simons, K., Schwille, P., 2012. Biochim. Biophys. Acta 1818 (7), 1777–1784.
Simons, K., Gerl, M.J., 2010. Nat. Rev. Mol. Cell Biol. 11 (10), 688–699.
Sjoelander, S., Urbaniczky, C., 1991. Anal. Chem. 63 (20), 2338–2345.
Skaug, M.J., Longo, M.L., Faller, R., 2011. J. Phys. Chem. B 115 (26), 8500–8505.
Sprong, H., van der Sluijs, P., van Meer, G., 2001. Nat. Rev. Mol. Cell Biol. 2 (7), 504–513.
Suh, J.-H., Lee, S.-W., Ryu, Y.-S., Sohn, Y., Lee, S.-D., 2014. Mol. Cryst. Liq. Cryst. 600 (1), 81–87.
Thatcher, J.D., 2013. Sci. Signal. 6 (271), tr4.
Veatch, S.L., Leung, S.S., Hancock, R.E., Thewalt, J.L., 2007. J. Phys. Chem. B 111 (3), 502–504.
Vijayendran, R.A., Ligler, F.S., Leckband, D.E., 1999. Anal. Chem. 71 (23), 5405–5412.
Waring, P., Lambert, D., Sjaarda, A., Hurne, A., Beaver, J., 1999. Cell Death Differ. 6 (7), 624–637.
Winssinger, N., Harris, J.L., Backes, B.J., Schultz, P.G., 2001. Angew. Chem. Int. Ed. 40 (17), 3152–3155.
Yang, L., Shirahata, N., Saini, G., Zhang, F., Pei, L., Asplund, M.C., Kurth, D.G., Ariga, K., Sautter, K., Nakanishi, T., Smentkowski, V., Linford, M.R., 2009. Langmuir 25 (10), 5674–5683.
Yee, C.K., Amweg, M.L., Parikh, A.N., 2004. Adv. Mater. 16 (14), 1184–1189.
Yoon, T.-Y., Jeong, C., Lee, S.-W., Kim, J.H., Choi, M.C., Kim, S.-J., Kim, M.W., Lee, S.-D., 2006. Nat. Mater. 5 (4), 281–285.
Yuk, J.S., Ha, K.-S., 2005. Exp. Mol. Med. 37, 1–10.
Yun, H., Lee, I.-M., Im, S.H., Lee, S.-Y., Lee, B., 2011. Nanotechnology 23 (1), 015306.
Zhao, J., Wu, J., Shao, H., Kong, F., Jain, N., Hunt, G., Feigenson, G., 2007. Biochim. Biophys. Acta 1768 (11), 2777–2786.